

This is a pre-print version of the paper. Please cite the final version of the paper:

G. Di Martino, A. Iodice, D. Riccio "Closed-Form Anisotropic Polarimetric Two-Scale Model for Fast Evaluation of Sea Surface Backscattering", *IEEE Trans. Geosci. Remote Sens.*, vol. 57, no. 8, pp. 6182-6194, Aug. 2019. DOI: [10.1109/TGRS.2019.2904761](https://doi.org/10.1109/TGRS.2019.2904761).

IEEE Copyright notice. © 2019 IEEE. Personal use of this material is permitted. Permission from IEEE must be obtained for all other uses, in any current or future media, including reprinting/republishing this material for advertising or promotional purposes, creating new collective works, for resale or redistribution to servers or lists, or reuse of any copyrighted component of this work in other works.

Closed-Form Anisotropic Polarimetric Two-Scale Model for Fast Evaluation of Sea Surface Backscattering

Gerardo Di Martino¹, Senior Member, IEEE, Antonio Iodice¹, Senior Member, IEEE, and Daniele Riccio¹, Fellow, IEEE

Abstract—The polarimetric two-scale model (PTSM) was introduced a few years ago as an electromagnetic scattering model to be used within algorithms for soil moisture retrieval from polarimetric synthetic aperture radar (SAR) data. PTSM inherits the ability to account for depolarization effects from the original two-scale model (TSM), and, with respect to the latter, it has the advantage to provide closed-form expressions of the elements of the covariance matrix that hold for moderate large-scale surface slopes. This allows a very fast evaluation of scattering, since numerical integration needed by the original TSM is avoided. The TSM, also called composite model (CM), has been extensively used to study scattering from the sea surface, so that it is natural to explore the use of PTSM for the same purpose. However, in its current formulation, PTSM assumes that large-scale surface slope distribution and small-scale roughness spectrum are isotropic. This is not realistic for the sea surface, for which anisotropy is dictated by the wind direction. Accordingly, we here extend PTSM to account for surface roughness anisotropy, so obtaining the anisotropic PTSM (A-PTSM). In addition, as a second contribution, we provide A-PTSM expressions also in the circular polarization basis, which may be useful for some SAR sensor polarimetric configurations. Finally, we compare A-PTSM results with sea surface scattering measurements available in the literature and with results of the second-order small-slope approximation (SSA2). In particular, as a third original contribution of this paper, an analytical closed-form expression of the ratio of crosspolarized normalized radar cross sections (NRCSs) obtained by SSA2 and A-PTSM is provided.

Index Terms—Polarimetry, scattering from rough surfaces, sea surface.

I. INTRODUCTION

THE two-scale model (TSM), also called composite model (CM), [1], [2] has been extensively used for computation of scattering from rough surfaces, and, in particular, from sea surfaces, see [3]–[5]. According to TSM, the rough surface is modeled as the superposition of a large-scale (or low-frequency) roughness, which includes surface spectral components with wavenumbers lower than a properly chosen cutoff wavenumber, and a small-scale (or high-frequency) roughness, which encompasses surface spectral components

with wavenumbers higher than the cutoff wavenumber. The latter must be sufficiently smaller than the electromagnetic wavenumber, and sufficiently larger than 2π times the inverse of the sensor resolution, so that a certain degree of arbitrariness is implied in its choice. Scattering from large-scale roughness is evaluated by using the geometrical optics (GO) approximation; it is dominant at near-specular directions (in backscattering, at small incidence angles) and the elements of the polarimetric covariance matrix, including the normalized radar cross sections (NRCS) at different polarizations, turn out to be dependent on the large-scale surface slope probability density function (pdf). Conversely, scattering from the small-scale roughness is computed by evaluating the scattering from a randomly tilted rough facet via the small perturbation method (SPM), and then averaging the obtained NRCS over the facet random slopes, statistically distributed according to the large-scale surface slope pdf. Backscattering from small-scale roughness is dominant at intermediate incidence angles and the elements of the polarimetric covariance matrix, including the NRCS, mainly depend on the small-scale roughness power spectral density (PSD). It must be noted that no depolarization effect can be obtained by the TSM if the facet random tilt is not accounted for, so that averaging over the facet random slopes is a necessary step for a polarimetric scattering analysis via the TSM.

Although GO and SPM provide closed-form expressions of NRCS, accurate averaging over surface slopes requires the numerical evaluation of the corresponding integral, so that no closed-form expression for the NRCS (and for the other elements of the polarimetric covariance matrix) can be obtained via the TSM as it was originally formulated [1], [2] and usually employed [3]–[5] (unless very raw approximations are done, as in [1]). However, a closed-form formulation of TSM was introduced a few years ago in [6] and [7], where it was called polarimetric TSM (PTSM). PTSM inherits the ability to account for crosspolarization and depolarization effects from the original TSM, and, with respect to the latter, it has the advantage to provide closed-form expressions of the elements of the covariance matrix that hold for moderate large-scale surface slopes [6], [7]. This is achieved by performing a second order expansion of the tilted-facet SPM expressions with respect to large-scale surface slopes before performing the average operation [6], [7].

PTSM was originally introduced as a fast method for the computation of backscattering from bare soils, to be used

Manuscript received January 24, 2019; revised February 27, 2019; accepted March 10, 2019. (Corresponding author: Gerardo Di Martino.)

The authors are with the Dipartimento di Ingegneria Elettrica e delle Tecnologie dell'Informazione, Università di Napoli Federico II, 80125 Naples, Italy (e-mail: gerardo.dimartino@unina.it; iodice@unina.it; daniele.riccio@unina.it).

Color versions of one or more of the figures in this paper are available online at <http://ieeexplore.ieee.org>.

Digital Object Identifier 10.1109/TGRS.2019.2904761

within algorithms for soil moisture retrieval from polarimetric synthetic aperture radar (SAR) data [6]–[8]. Nevertheless, since TSM has been extensively used to study backscattering from the sea surface, it is natural to explore the use of PTSM for the same purpose. However, in its current formulation PTSM assumes that large-scale surface slope distribution and small-scale roughness PSD are isotropic, which is not realistic for the sea surface. In fact, the variance of sea surface slope along the upwind (or downwind) direction is usually higher than the one along the crosswind direction. Therefore, slopes along range and azimuth directions turn out to have different variances and to be correlated, and their variances and correlation coefficient can be expressed in terms of upwind and crosswind variances and of the angle between wind and ground range directions, as we illustrate in Section II. Similarly, the small-scale PSD shows an anisotropy dictated by the wind direction. Accordingly, we here extend PTSM to account for sea surface anisotropy, and this is the first contribution of this paper. We call this new proposed model the anisotropic (or advanced) PTSM (A-PTSM), see Section III. In addition, as a second contribution, we provide A-PTSM expressions also in the circular polarization basis, which may be useful for some SAR sensor polarimetric configurations.

A limitation of TSM and A-PTSM is that they only account for depolarization effect due to surface tilting, whereas they ignore depolarization due to multiple scattering, so that it is expected that they underestimate this effect [9]. A more accurate model that also accounts for multiple scattering is the second-order small-slope approximation (SSA2) [9]. However, this higher accuracy is paid by the fact that SSA2 requires a computationally demanding numerical evaluation of fourfold integrals. Comparisons of numerical evaluations of TSM and SSA2 performed in [9] showed that generally they are in good agreement, except for the crosspolarized NRCS which, in the considered cases, is underestimated by TSM of two to four dB with respect to the SSA2 value. Since only numerical evaluations of both SSA2 and TSM were available in [9], these comparisons were made only for specific surface parameters, incidence angles and frequencies, so that no general conclusion can be drawn. Fortunately, in [10], an analytical approximation of SSA2 (SSA2-A) was obtained (although for the crosspolarized NRCS only), and it was shown that it is in very good agreement with exact SSA2 for moderate slopes and intermediate incidence angles. This allows us to obtain, as a third contribution of this paper, an analytical closed-form expression of the ratio of crosspolarized NRCSs obtained by SSA2-A and A-PTSM, which allows us to draw some general conclusions on the approximate agreement of results from the two methods, see Section IV.

Finally, comparisons of A-PTSM results with measured data obtained from the literature are presented, see Section IV.

II. SEA SURFACE DESCRIPTION

In order to evaluate sea surface scattering via the TSM, we need to specify the PSD of the height profile of the small-scale roughness and the pdf of the slopes of the large-scale roughness, with a cutoff wavenumber κ_{cut} of the order of (but

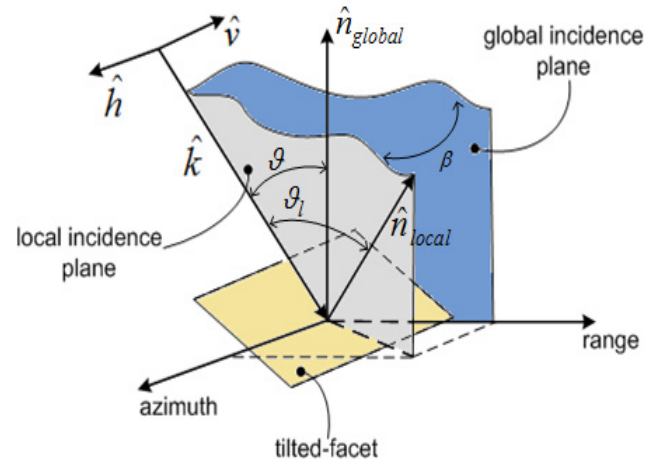


Fig. 1. Geometry of the scattering problem for a tilted facet.

smaller than) the wavenumber k of the incident microwave signal. In the following, we will make use of a reference system whose axes in the horizontal plane are the ground-range (or in-plane) and azimuth (or out-of-plane) directions. The ground-range direction is defined as the intersection of incidence and horizontal planes, whereas the azimuth direction is perpendicular to the incidence plane, see Fig. 1.

A. Small-Scale Roughness

With regard to the PSD of the small-scale roughness heights, we use the high-frequency part of the directional Elfouhaily spectrum [11]

$$W_{2D}(\kappa, \varphi) = W(\kappa)\Phi(\kappa, \varphi) \quad (1)$$

where κ is the amplitude of the surface wavenumber vector and φ is the angle between the surface wavenumber vector and the ground-range direction; $W(\kappa)$ is the omnidirectional part of the spectrum, expressed as¹

$$W(\kappa) = \frac{\pi \alpha_m c_m}{c \kappa^4} \exp \left[-\frac{1}{4} \left(\frac{\kappa}{\kappa_m} - 1 \right)^2 \right] \quad (2)$$

where

$$\alpha_m = \begin{cases} 0.01[1 + \ln(u^*/c_m)], & \text{for } u^* \leq c_m \\ 0.01[1 + 3 \ln(u^*/c_m)], & \text{for } u^* > c_m \end{cases} \quad (3)$$

$$\kappa_m = 363 \text{ m}^{-1} \quad c_m = 0.23 \text{ m/s}$$

c is the sea-wave phase velocity, computed from the sea surface dispersion relation as

$$c = \sqrt{\frac{g}{\kappa} \left[1 + \left(\frac{\kappa}{\kappa_m} \right)^2 \right]} \quad (4)$$

g being the gravity acceleration, equal to 9.81 m/s^2 , and u^* is the friction velocity, related to the wind velocity at 10 m height u_{10} by the following relation [11], [12]:

$$u^* = \sqrt{C_d} u_{10} \quad (5)$$

¹By following [6], in our convention, the factor $1/(2\pi)$ appears in the 1-D inverse Fourier Transform, at variance with the convention used in [11], where the factor $1/(2\pi)$ appears in the 1-D direct Fourier Transform.

with

$$C_d = \begin{cases} 1.205 \cdot 10^{-3}, & \text{for } 4 \leq u_{10} < 11 \text{ m/s} \\ (0.49 + 0.065u_{10})10^{-3}, & \text{for } 11 \leq u_{10} \leq 25 \text{ m/s} \end{cases} \quad (6)$$

finally, $\Phi(\kappa, \varphi)$ is the angular spreading function, given by [11]

$$\Phi(\kappa, \varphi) = 1 + \Delta(\kappa) \cos[2(\varphi_w - \varphi)] \quad (7)$$

where

$$\Delta(\kappa) = \tanh[0.173 + 4(c/c_p)^{2.5} + a_m(c_m/c)^{2.5}] \quad (8)$$

with $c_p \cong u_{10}/0.84$ and $a_m = 0.13u^*/c_m$, and φ_w is the angle between wind and ground-range directions.

It is useful to note that the range of surface wavenumbers of interest here spans from a few tens of rad/m (for L-band sensors) to a few hundreds of rad/m (for Ku-band sensors). In this range of wavenumbers, the exponential factor in (2) is practically constant and very close to unity, and sea-wave phase velocity can be approximated as $c \cong \sqrt{g/\kappa}$. Accordingly, a useful approximation of the omnidirectional part of the spectrum is

$$W(\kappa) \cong \frac{\pi \alpha_m c_m}{\sqrt{g} \kappa^{3.5}} \exp \left[-\frac{1}{4} \left(\frac{\kappa_0}{\kappa_m} - 1 \right)^2 \right] \quad (9)$$

with κ_0 being a fixed wavenumber in the range of interest. Equation (9) is coincident with the isotropic power-law PSD used in [6], with Hurst coefficient $H_t = 0.75$ and amplitude coefficient S_0 given by

$$S_0 = \frac{\pi \alpha_m c_m}{\sqrt{g}} \exp \left[-\frac{1}{4} \left(\frac{\kappa_0}{\kappa_m} - 1 \right)^2 \right]. \quad (10)$$

In addition, in the considered range of wavenumbers $\Delta(\kappa)$ turns out to be weakly dependent on κ and much smaller than unity, except for strong winds, so that the angular spreading function may be approximated as

$$\Phi(\kappa, \varphi) \cong \Phi(\varphi) = 1 + \Delta(\kappa_0) \cos[2(\varphi_w - \varphi)]. \quad (11)$$

Comparison of exact, (2) and (7), and approximate, (9) and (11), PSDs is shown in Fig. 2 for different wind directions and for $u_{10} = 15$ m/s. For higher wind speeds, of the order of 20 m/s or larger, the approximation is less accurate. However, at those wind speeds other nonmodeled phenomena, such as breaking waves, have a more significant effect on accuracy of scattering calculations. In addition, as it will be better explained in Section III-C, in scattering evaluations, we will use approximate expressions (9) and (11) only for the computation of higher order terms of power series expansions, whereas for the dominant terms, we will use exact expressions (2) and (7).

B. Large-Scale Roughness

As originally shown in [13], sea surface slopes along up-wind and crosswind directions, s_{up} and s_{cross} , are, with good approximation, zero-mean independent Gaussian random variables with variances σ_{up}^2 and σ_{cross}^2 , respectively.

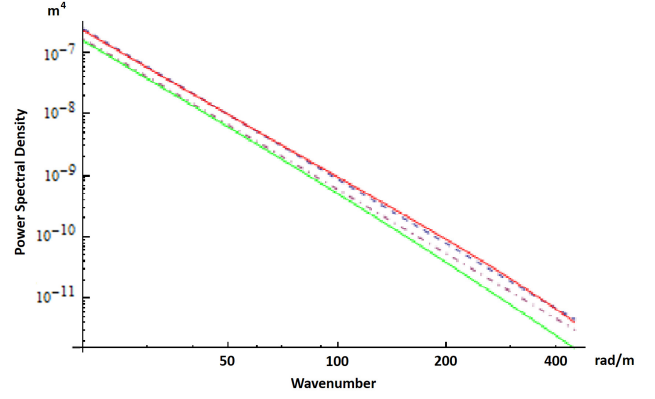


Fig. 2. Exact (solid lines) and power-law approximated (dashed lines) directional spectra for $\varphi_w - \varphi$ equal to 0° (upper lines) and 90° (lower lines); $u_{10} = 15$ m/s, $\kappa_0 = 75$ rad/m.

Such variances were computed in [13] based on measurements of sunlight reflection, thus including both large-scale and small-scale roughness. To obtain an evaluation of the slope variances of the large-scale roughness only, a possibility is to compute them from the sea surface PSD

$$\sigma_{\text{up,cross}}^2 = \frac{1}{4\pi^2} \int_0^{2\pi} \int_0^{\kappa_{\text{cut}}} \kappa^2 \cos^2(\varphi - \varphi_w - \psi_{\text{up,cross}}) \times W_{2D}(\kappa, \varphi) \kappa d\kappa d\varphi \quad (12)$$

where $\psi_{\text{up}} = 0$, $\psi_{\text{cross}} = \pi/2$ and the whole (i.e., both its high- and small-frequency parts) directional PSD must be used. This has two drawbacks: first of all, the obtained result depends on the choice of the PSD expression and of the cutoff wavenumber; in addition, the numerical evaluation of a twofold integral is needed. To avoid these drawbacks, we here use the semiempirical evaluation of [14], based on measurements of sea surface scattering of global navigation satellite system (GNSS) L-band signals (carrier frequency: 1.5 GHz) along near-specular directions and on the assumption of GO scattering (which is very reasonable for near-specular directions)

$$\begin{aligned} \sigma_{\text{up}0}^2 &= 0.45[0.00316f(u_{10})] \\ \sigma_{\text{cross}0}^2 &= 0.45[0.003 + 0.00192f(u_{10})] \end{aligned} \quad (13)$$

where u_{10} is the wind speed at 10-m height, measured in m/s, and

$$\begin{aligned} f(u_{10}) &= u_{10} \quad \text{for } 0 < u_{10} \leq 3.49 \\ f(u_{10}) &= 6 \ln(u_{10}) \quad \text{for } 3.49 < u_{10} \leq 46 \\ f(u_{10}) &= 0.411 u_{10} \quad \text{for } 46 < u_{10}. \end{aligned} \quad (14)$$

Then, to obtain large-scale roughness slope variances for a different frequency of the microwave range, we correct the 1.5-GHz values of (13) as follows:

$$\begin{aligned} \sigma_{\text{up,cross}}^2 &\cong \sigma_{\text{up}0,\text{cross}0}^2 + \frac{1}{4\pi^2} \int_0^{2\pi} \int_{\kappa_{\text{cut}0}}^{\kappa_{\text{cut}}} \kappa^2 \cos^2(\varphi - \varphi_w - \psi_{\text{up,cross}}) \\ &\quad \times W(\kappa) \Phi(\varphi) \kappa d\kappa d\varphi \\ &= \sigma_{\text{up}0,\text{cross}0}^2 + \frac{S_0}{2\pi} \left(1 \pm \frac{\Delta(\kappa_0)}{2} \right) (\sqrt{\kappa_{\text{cut}}} - \sqrt{\kappa_{\text{cut}0}}) \end{aligned} \quad (15)$$

where $\kappa_{\text{cut}0}$ is the cutoff wavenumber at 1.5 GHz, and the approximate expressions of (9) and (11) are used for $W(\kappa)$ and $\Phi(\varphi)$, respectively, since the integral only spans values of κ for which they are accurate. In (15), we will use $\kappa_{\text{cut}} = k/2$, but the slope variance values in (15) only slightly depend on this choice, since the bulk of the evaluation is based on the semiempirical values of (13). For the same reason, the approximations in (9) and (11) have a negligible effect on the obtained slope variance values. In addition, thanks to them no numerical evaluation of integrals is needed.

As we will see in Section III, for scattering computation purposes, it is necessary to specify the pdf of surface slopes along ground-range (or in-plane) and azimuth (or out-of-plane) directions, s_r and s_a . By recalling that φ_w is the angle between wind and ground-range directions, and noting that $(s_{\text{up}}, s_{\text{cross}})$ and (s_r, s_a) are the components of the surface gradient vector in two reference systems rotated by the angle φ_w , we get

$$\begin{bmatrix} s_r \\ s_a \end{bmatrix} = \underline{\underline{R_2}}(\varphi_w) \begin{bmatrix} s_{\text{up}} \\ s_{\text{cross}} \end{bmatrix} \quad (16)$$

wherein

$$\underline{\underline{R_2}}(\varphi_w) = \begin{bmatrix} \cos \varphi_w & \sin \varphi_w \\ -\sin \varphi_w & \cos \varphi_w \end{bmatrix} \quad (17)$$

is the unitary rotation matrix. By using (16) and (17), we readily get that s_r and s_a are zero-mean jointly Gaussian random variables with variances

$$\begin{aligned} \sigma_r^2 &= \sigma_{\text{up}}^2 \cos^2 \varphi_w + \sigma_{\text{cross}}^2 \sin^2 \varphi_w \\ &= \frac{1}{2} [\sigma_{\text{up}}^2 + \sigma_{\text{cross}}^2 + (\sigma_{\text{up}}^2 - \sigma_{\text{cross}}^2) \cos 2\varphi_w] \\ \sigma_a^2 &= \sigma_{\text{cross}}^2 \cos^2 \varphi_w + \sigma_{\text{up}}^2 \sin^2 \varphi_w \\ &= \frac{1}{2} [\sigma_{\text{up}}^2 + \sigma_{\text{cross}}^2 - (\sigma_{\text{up}}^2 - \sigma_{\text{cross}}^2) \cos 2\varphi_w] \end{aligned} \quad (18)$$

and correlation coefficient

$$\rho = \frac{1}{2} \sin 2\varphi_w \frac{\sigma_{\text{cross}}^2 - \sigma_{\text{up}}^2}{\sigma_r \sigma_a}. \quad (19)$$

We explicitly note that if up-wind and crosswind slope variances are equal, then range and azimuth slopes are independent and with equal variances, too, and isotropy is recovered. In addition, range and azimuth slopes are independent also if wind direction is along range or azimuth ($\varphi_w = 0$, or $\varphi_w = \pi$, or $\varphi_w = \pm\pi/2$).

III. ANISOTROPIC PTSM

According to the TSM, the elements of the polarimetric covariance matrix, $R_{pq,rs}$, can be written as the sum of the large-scale roughness contribution, $R_{pq,rs}^{\text{GO}}$, computed via the GO, and the small-scale roughness contribution, $\langle R_{pq,rs}^{\text{SPM}} \rangle_{s_a, s_r}$, computed as the SPM scattering from a tilted rough facet, averaged over the large-scale surface slopes

$$R_{pq,rs} = R_{pq,rs}^{\text{GO}} + \langle R_{pq,rs}^{\text{SPM}} \rangle_{s_a, s_r} \quad (20)$$

where the subscripts p, q, r, s may each stand for h (horizontal polarization) or v (vertical polarization), and the symbol $\langle \cdot \rangle_{s_a, s_r}$ represents the statistical mean with respect to the random variables s_a and s_r . Note that $R_{pq,pq}$ is the NRCS σ_{pq}^0 at pq polarization.

A. GO Scattering From the Large-Scale Roughness

For the large-scale backscattering contribution, we employ the usual GO expression

$$R_{pq,rs}^{\text{GO}} = \begin{cases} \frac{|\Gamma|^2}{2\sigma_a\sigma_r\sqrt{1-\rho^2}\cos^4\vartheta} \exp\left\{-\frac{\tan^2\vartheta}{2(1-\rho^2)\sigma_r^2}\right\} & \text{if } p=q \text{ and } r=s \\ 0, & \text{otherwise} \end{cases} \quad (21)$$

where ϑ is the (global) incidence angle, see Fig. 1, and Γ is the Fresnel reflection coefficient at normal incidence

$$\Gamma = \frac{1 - \sqrt{\varepsilon}}{1 + \sqrt{\varepsilon}} \quad (22)$$

with ε being the sea complex relative permittivity. Note that no depolarization is present in this contribution, and that also nonnull copolarized terms become negligible as soon as the tangent of the incidence angle is a few times the root-mean-square (rms) range slope.

B. SPM Scattering From a Tilted Rough Facet

With respect to computation of backscattering from small-scale roughness, PTSM [6] uses an approach slightly different from the original TSM [1]–[5]. In fact, instead of trying to express the SPM backscattering from a locally tilted rough facet directly in terms of surface slopes, or tilt angles, it first formulates the SPM backscattering in terms of local incidence angle ϑ_l and local incidence plane rotation angle β , see Fig. 1, and then it uses available relations between these parameters and surface slopes [6], [15]

$$\begin{cases} \tan \beta = \frac{s_a}{\sin \vartheta - s_r \cos \vartheta} \\ \cos \vartheta_l = \frac{\cos \vartheta + s_r \sin \vartheta}{\sqrt{1 + s_a^2 + s_r^2}}. \end{cases} \quad (23)$$

Here, we follow this procedure, whose advantage will be clearer in Section III-C. With respect to original PTSM, novelties are that here we use anisotropic statistics for s_r and s_a , see Section II-B, and an anisotropic small-scale roughness spectrum, see Section II-A. To cope with an anisotropic spectrum, we need to account not only for the local incidence and rotation angles ϑ_l and β , but also for the local ground-range direction, i.e., the intersection of the local incidence plane and the tilted facet. The local ground-range direction is characterized by the angle φ_l between its projection on the horizontal plane and the (global) ground-range direction, as defined in Section II. The relation between φ_l and s_a, s_r can also be evaluated, but, as we will see in the following, its full expression is not needed here.

The SPM expression of the covariance matrix elements of the tilted facet is [6], [7]

$$R_{pq,rs}^{\text{SPM}} = \frac{4}{\pi} k^4 \cos^4 \vartheta_l \chi_{pq}(\vartheta_l, \beta) \chi_{rs}^*(\vartheta_l, \beta) W_{2D}(2k \sin \vartheta_l, \varphi_l) \quad (24)$$

where k is the electromagnetic wavenumber

$$\underline{\underline{\chi}}(\vartheta_l, \beta) = \underline{\underline{R_2}}(\beta) \cdot \begin{pmatrix} F_h(\vartheta_l) & 0 \\ 0 & F_v(\vartheta_l) \end{pmatrix} \cdot \underline{\underline{R_2}}^{-1}(\beta) \quad (25)$$

with $R_2(\beta)$ accounting for the rotation of the local polarization reference system with respect to the global one, and F_h and F_v are the Bragg coefficients for horizontal and vertical polarizations, respectively,

$$\begin{cases} F_h = \frac{\cos \vartheta_l - \sqrt{\varepsilon - \sin^2 \vartheta_l}}{\cos \vartheta_l + \sqrt{\varepsilon - \sin^2 \vartheta_l}} \\ F_v = (\varepsilon - 1) \frac{\sin^2 \vartheta_l - \varepsilon(1 + \sin^2 \vartheta_l)}{(\varepsilon \cos \vartheta_l + \sqrt{\varepsilon - \sin^2 \vartheta_l})^2} \end{cases} \quad (26)$$

By using (25) and (1), we can write (24) more explicitly as

$$\begin{cases} \sigma_{hh}^{0\text{SPM}} = \frac{4}{\pi} k^4 \cos^4 \vartheta_l W(2k \sin \vartheta_l) \Phi(2k \sin \vartheta_l, \varphi_l) \\ \quad \times [|F_h(\vartheta_l)|^2 \cos^4 \beta + |F_v(\vartheta_l)|^2 \sin^4 \beta \\ \quad + 2\text{Re}\{F_h(\vartheta_l)F_v^*(\vartheta_l)\} \sin^2 \beta \cos^2 \beta] \\ \sigma_{vv}^{0\text{SPM}} = \frac{4}{\pi} k^4 \cos^4 \vartheta_l W(2k \sin \vartheta_l) \Phi(2k \sin \vartheta_l, \varphi_l) \\ \quad \times [|F_v(\vartheta_l)|^2 \cos^4 \beta + |F_h(\vartheta_l)|^2 \sin^4 \beta \\ \quad + 2\text{Re}\{F_v(\vartheta_l)F_h^*(\vartheta_l)\} \sin^2 \beta \cos^2 \beta] \\ \sigma_{hv}^{0\text{SPM}} = \frac{4}{\pi} k^4 \cos^4 \vartheta_l W(2k \sin \vartheta_l) \Phi(2k \sin \vartheta_l, \varphi_l) \\ \quad \times [|F_h(\vartheta_l)|^2 + |F_v(\vartheta_l)|^2 - 2\text{Re}\{F_h(\vartheta_l)F_v^*(\vartheta_l)\}] \\ \quad \times \sin^2 \beta \cos^2 \beta \\ R_{hh,vv}^{\text{SPM}} = \frac{4}{\pi} k^4 \cos^4 \vartheta_l W(2k \sin \vartheta_l) \Phi(2k \sin \vartheta_l, \varphi_l) \\ \quad \times \{ F_h(\vartheta_l)F_v^*(\vartheta_l) \cos^4 \beta + F_v(\vartheta_l)F_h^*(\vartheta_l) \sin^4 \beta \\ \quad + [|F_h(\vartheta_l)|^2 + |F_v(\vartheta_l)|^2] \sin^2 \beta \cos^2 \beta \} \\ R_{hh,hv}^{\text{SPM}} = \frac{4}{\pi} k^4 \cos^4 \vartheta_l W(2k \sin \vartheta_l) \Phi(2k \sin \vartheta_l, \varphi_l) \\ \quad \times \{ [F_h(\vartheta_l)F_v^*(\vartheta_l) - |F_h(\vartheta_l)|^2] \cos^3 \beta \sin \beta \\ \quad + [|F_v(\vartheta_l)|^2 - F_v(\vartheta_l)F_h^*(\vartheta_l)] \sin^3 \beta \cos \beta \} \\ R_{hv,vv}^{\text{SPM}} = \frac{4}{\pi} k^4 \cos^4 \vartheta_l W(2k \sin \vartheta_l) \Phi(2k \sin \vartheta_l, \varphi_l) \\ \quad \times \{ [|F_v(\vartheta_l)|^2 - F_h(\vartheta_l)F_v^*(\vartheta_l)] \cos^3 \beta \sin \beta \\ \quad + [F_v(\vartheta_l)F_h^*(\vartheta_l) - |F_h(\vartheta_l)|^2] \sin^3 \beta \cos \beta \} \\ R_{vv,hh}^{\text{SPM}} = R_{hh,vv}^{\text{SPM}*}, \quad R_{hv,hh}^{\text{SPM}} = R_{hh,hv}^{\text{SPM}*}, \quad R_{vv,hv}^{\text{SPM}} = R_{hv,vv}^{\text{SPM}*} \end{cases} \quad (27)$$

Equation (27) shows that the elements of the covariance matrix can be written as the sum of terms of the kind $\Theta_{pq}(\vartheta_l) \Phi(2k \sin \vartheta_l, \varphi_l) B_n(\beta)$, where

$$\Theta_{pq}(\vartheta_l) = \frac{4}{\pi} k^4 \cos^4 \vartheta_l W(2k \sin \vartheta_l) F_p(\vartheta_l) F_q^*(\vartheta_l). \quad (28)$$

$\Phi(2k \sin \vartheta_l, \varphi_l)$ is given by (13) and $B_n(\beta) = \cos^{4-n} \beta \sin^n \beta$, with n integer and $0 \leq n \leq 4$.

C. Taylor Series Expansion

Taylor power series expansion of the covariance matrix elements in (27) with respect to s_a and s_r can be readily obtained once expansions of $\Theta_{pq}(\vartheta_l)$, $\Phi(2k \sin \vartheta_l, \varphi_l)$, and $B_n(\beta)$ are performed.

The series expansion of $\Theta_{pq}(\vartheta_l)$ up to the second order can be expressed as

$$\begin{aligned} \Theta_{pq}(\vartheta_l) &\cong \Theta_{pq}(\vartheta) + C_{0,1}^{pq} s_r + C_{2,0}^{pq} s_a^2 + C_{0,2}^{pq} s_r^2 \\ &= \Theta_{pq}(\vartheta) \left[1 + \frac{C_{0,1}^{pq} s_r + C_{2,0}^{pq} s_a^2 + C_{0,2}^{pq} s_r^2}{\Theta_{pq}(\vartheta)} \right] \end{aligned} \quad (29)$$

where

$$C_{k,n-k}^{pq} = \frac{1}{n!} \binom{n}{k} \frac{\partial^n \Theta_{pq}(\vartheta_l)}{\partial s_a^k \partial s_r^{n-k}} \Big|_{s_a=s_r=0} \quad (30)$$

and the derivatives in (30) can be computed by applying the chain rule to (28) and the second of (23). This allows immediately recognizing that $C_{1,0}^{pq} = C_{1,1}^{pq} = 0$, since

$$\frac{\partial \cos \vartheta_l}{\partial s_a} \Big|_{s_a=s_r=0} = \frac{\partial^2 \cos \vartheta_l}{\partial s_a \partial s_r} \Big|_{s_a=s_r=0} = 0. \quad (31)$$

In addition, if to compute the derivatives in (30) we use the power-law approximate expression of $W(\kappa)$ given in (9), then we obtain the analytical closed-form expressions of $C_{2,0}^{pq}$, $C_{0,2}^{pq}$ reported in [6, Appendix B], and of $C_{0,1}^{pq}$ reported in Appendix A. We explicitly underline that the approximate expression of $W(\kappa)$ given in (9) is only used to compute the derivatives in (30), whereas the zero-order term $\Theta_{pq}(\vartheta)$ is computed by using the exact expression of $W(\kappa)$ given in (2).

With regard to $\Phi(2k \sin \vartheta_l, \varphi_l)$, we assume that its first-order series expansion is sufficient, because second-order terms include a factor $\Delta(\kappa)$ that is usually much smaller than unity (see Section II), so that they can be neglected; in addition, in computing the derivatives appearing in the series expansion, we use the approximate expression of $\Phi(\kappa, \varphi_l)$ given in (11), so obtaining

$$\begin{aligned} &\Phi(2k \sin \vartheta_l, \varphi_l) \\ &\cong 1 + \Delta(2k \sin \vartheta) \cos 2\varphi_w \\ &\quad + 2\Delta(2k \sin \vartheta) \sin 2\varphi_w \frac{\partial \varphi_l}{\partial s_a} \Big|_{s_a=s_r=0} s_a \\ &= \Phi(2k \sin \vartheta, 0) \left(1 + \frac{2\Delta(2k \sin \vartheta) \sin 2\varphi_w}{\Phi(2k \sin \vartheta, 0)} \frac{\partial \varphi_l}{\partial s_a} \Big|_{s_a=s_r=0} s_a \right) \end{aligned} \quad (32)$$

where we have again used the chain rule and we have exploited the fact that $(\partial \varphi_l / \partial s_r)|_{s_a=s_r=0} = 0$, since $\varphi_l = 0$ for any s_r if $s_a = 0$. In Section III-D, we will see that the term involving $(\partial \varphi_l / \partial s_a)|_{s_a=s_r=0}$ is canceled by the average operation, so that its expression is of no concern here. Similar to the previous case, we explicitly underline that the approximate expression of $\Phi(\kappa, \varphi_l)$ given in (11) is only used to compute the derivatives appearing in the series expansion, whereas the zero-order term $\Phi(2k \sin \vartheta, 0)$ is computed by using the exact expression given in (7).

Finally, by using the first of (23) and recalling that

$$\sin \beta = \frac{\tan \beta}{\sqrt{1 + \tan^2 \beta}} \quad (33)$$

we obtain the following second-order expansion of $B_n(\beta)$:

$$B_n(\beta) \cong \begin{cases} 1 - \frac{2s_a^2}{\sin^2 \vartheta}, & \text{for } n = 0 \\ \frac{s_a}{\sin \vartheta} + \frac{s_a s_r \cot \vartheta}{\sin \vartheta}, & \text{for } n = 1 \\ \frac{s_a^2}{\sin^2 \vartheta}, & \text{for } n = 2 \\ 0, & \text{for } n > 2. \end{cases} \quad (34)$$

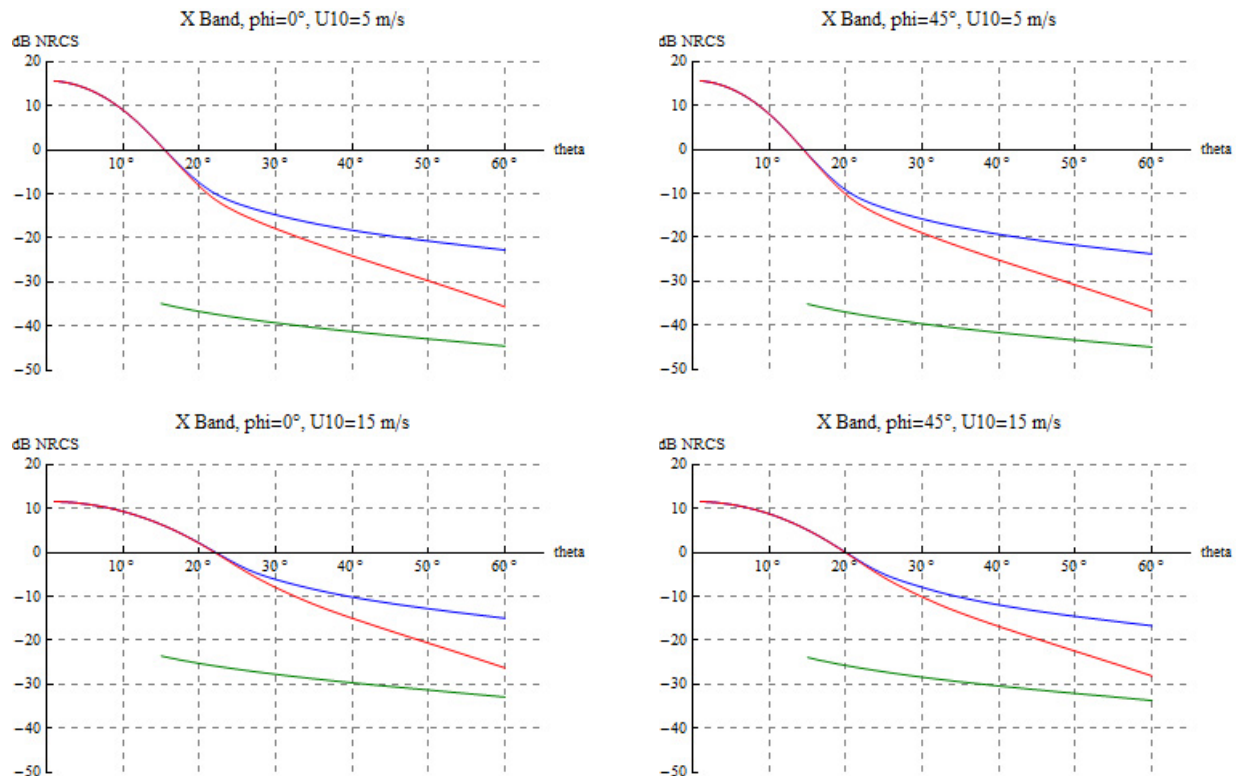


Fig. 3. NRCS at vv (upper, blue line), hh (middle, red line), and hv (lower, green line) polarizations as a function of the incidence angle ϑ at X-band (frequency = 10 GHz, $\epsilon = 61 - j45$) for a gentle breeze ($u_{10} = 5$ m/s) and a strong wind ($u_{10} = 15$ m/s), and for up-wind ($\varphi_w = 0$) and oblique ($\varphi_w = 45^\circ$) incidence.

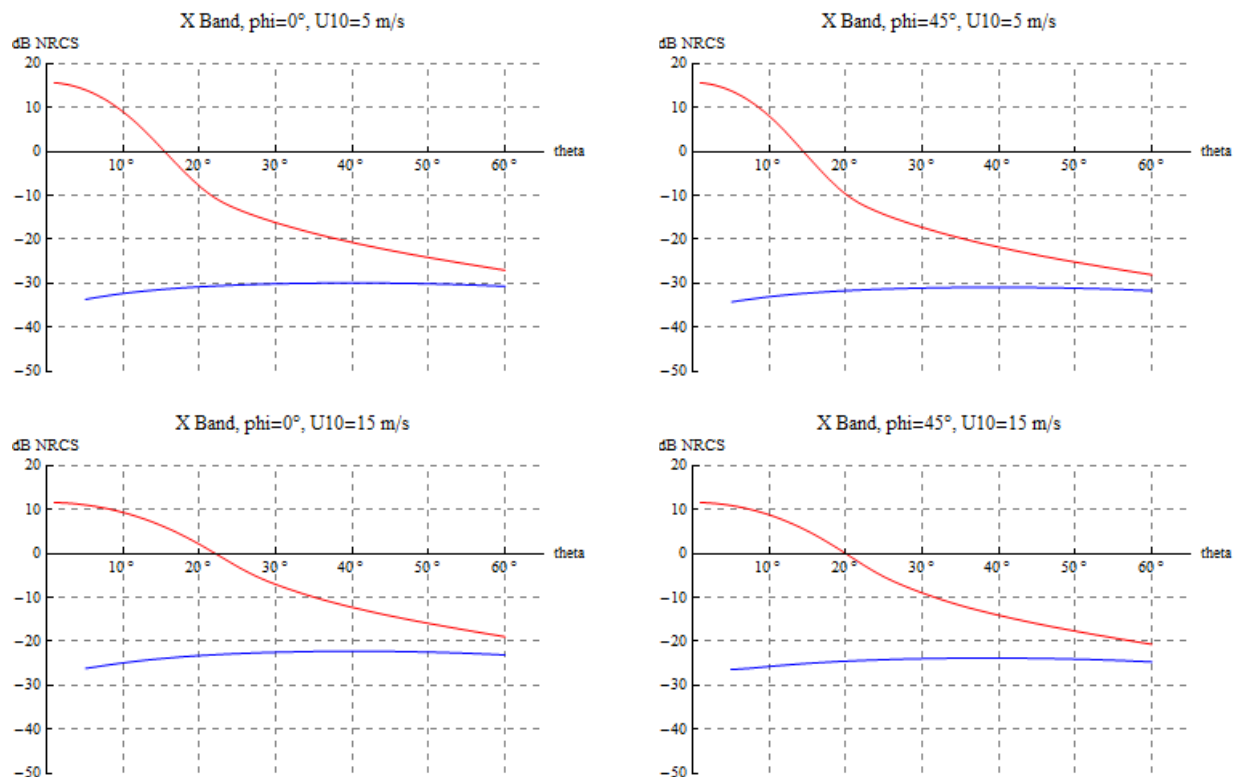


Fig. 4. NRCS at RR (lower, blue line) and RL (upper, red line) polarizations as a function of the incidence angle ϑ at X-band (frequency = 10 GHz, $\epsilon = 61 - j45$) for a gentle breeze ($u_{10} = 5$ m/s) and a strong wind ($u_{10} = 15$ m/s), and for up-wind ($\varphi_w = 0$) and oblique ($\varphi_w = 45^\circ$) incidence.

Note that these last expansions are not valid for small incidence angles ($\sin\vartheta \sim s_r$ or smaller), for which, anyway, SPM is not accurate.

D. Average Over Large-Scale Surface Slopes

Substituting (29), (32), and (34) into (27) and (28), neglecting terms of order higher than two (and those of order two that

include the factor Δ), averaging over s_a, s_r and recalling that $\langle s_a \rangle = \langle s_r \rangle = 0$, $\langle s_a^2 \rangle = \sigma_a^2$, $\langle s_r^2 \rangle = \sigma_r^2$, and $\langle s_a s_r \rangle = \rho \sigma_a \sigma_r$, we get

$$\begin{cases}
 \langle \sigma_{hh}^{0SPM} \rangle = \Theta_{hh}(\vartheta) \Phi(2k \sin \vartheta, 0) \\
 \quad \times \left[1 + \frac{C_{0,2}^{hh}}{\Theta_{hh}(\vartheta)} \sigma_r^2 + \left(\frac{C_{2,0}^{hh}}{\Theta_{hh}(\vartheta)} \right. \right. \\
 \quad \quad \left. \left. + 2 \frac{\text{Re}\{F_v(\vartheta)/F_h(\vartheta)\} - 1}{\sin^2 \vartheta} \right) \sigma_a^2 \right] \\
 \langle \sigma_{vv}^{0SPM} \rangle = \Theta_{vv}(\vartheta) \Phi(2k \sin \vartheta, 0) \\
 \quad \times \left[1 + \frac{C_{0,2}^{vv}}{\Theta_{vv}(\vartheta)} \sigma_r^2 + \left(\frac{C_{2,0}^{vv}}{\Theta_{vv}(\vartheta)} \right. \right. \\
 \quad \quad \left. \left. - 2 \frac{1 - \text{Re}\{F_h(\vartheta)/F_v(\vartheta)\}}{\sin^2 \vartheta} \right) \sigma_a^2 \right] \\
 \langle \sigma_{hv}^{0SPM} \rangle = \Theta_{hv}(\vartheta) \Phi(2k \sin \vartheta, 0) \frac{|F_v(\vartheta) - F_h(\vartheta)|^2}{F_h(\vartheta) F_v^*(\vartheta) \sin^2 \vartheta} \sigma_a^2 \\
 \langle R_{hh,vv}^{SPM} \rangle = \Theta_{hv}(\vartheta) \Phi(2k \sin \vartheta, 0) \\
 \quad \times \left[1 + \frac{C_{0,2}^{hv}}{\Theta_{hv}(\vartheta)} \sigma_r^2 + \left(\frac{C_{2,0}^{hv}}{\Theta_{hv}(\vartheta)} \right. \right. \\
 \quad \quad \left. \left. + \frac{F_h^*(\vartheta)/F_v^*(\vartheta) + F_v(\vartheta)/F_h(\vartheta) - 2}{\sin^2 \vartheta} \right) \sigma_a^2 \right] \\
 \langle R_{hh,hv}^{SPM} \rangle = \Theta_{hv}(\vartheta) \Phi(2k \sin \vartheta, 0) \\
 \quad \times \left[\frac{(1 - F_h^*(\vartheta)/F_v^*(\vartheta)) \cot \vartheta}{\sin \vartheta} + \frac{(C_{0,1}^{hv} - C_{0,1}^{hh})}{\Theta_{hv}(\vartheta) \sin \vartheta} \right] \rho \sigma_a \sigma_r \\
 \langle R_{hv,vv}^{SPM} \rangle = \Theta_{hv}(\vartheta) \Phi(2k \sin \vartheta, 0) \\
 \quad \times \left[\frac{(F_v(\vartheta)/F_h(\vartheta) - 1) \cot \vartheta}{\sin \vartheta} + \frac{(C_{0,1}^{vv} - C_{0,1}^{hv})}{\Theta_{hv}(\vartheta) \sin \vartheta} \right] \rho \sigma_a \sigma_r \\
 \langle R_{vv,hh}^{SPM} \rangle = \langle R_{hh,vv}^{SPM*} \rangle, \quad \langle R_{vv,hv}^{SPM} \rangle = \langle R_{hh,hv}^{SPM*} \rangle \\
 \langle R_{vv,hv}^{SPM} \rangle = \langle R_{hv,vv}^{SPM*} \rangle.
 \end{cases} \quad (35)$$

Expressions in (35) reduce to those of [6] and [7] if $\rho = 0$, $\sigma_a = \sigma_r$, and $\Phi(2k \sin \vartheta, 0) = 1$. In addition, the expressions in (35) reduce to the usual SPM ones if $\sigma_a = \sigma_r = 0$. Finally, note that $\Theta_{pq}(\vartheta)$ depends on wind velocity u_{10} , while $\Phi(2k \sin \vartheta, 0)$, σ_a , σ_r , and ρ depend on both wind velocity u_{10} and wind direction φ_w , see Section II. In particular, dependence of $\Theta_{pq}(\vartheta)$ on u_{10} is rather simple, since it is only via the parameter α_m in (2). With regard to wind direction, the main dependence is via $\Phi(2k \sin \vartheta, 0)$, and it is represented by oscillations of the kind $\cos(2\varphi_w)$. These are the dominant dependencies for copolarized NRCS, which can be also inferred using the standard SPM model. With regard to the crosspolarized NRCS, the dependence on u_{10} is also strongly related to the factor σ_a , so that a higher sensitivity to wind speed is expected for this term. As for wind direction, the oscillations of kind $\cos(2\varphi_w)$ due to $\Phi(2k \sin \vartheta, 0)$ are damped by the presence of the factor σ_a , which, according to (18), introduces another dependence of the kind $\cos(2\varphi_w)$, but with opposite sign. The proposed closed-form model also supports prediction of the behavior of the copolarized hh, vv

and crosspolarized vh, vv correlation coefficients, defined as

$$\rho_{hh,vv} = \frac{R_{hh,vv}}{\sqrt{\sigma_{hh}^0 \sigma_{vv}^0}}, \quad \rho_{vh,vv} = \frac{R_{vh,vv}}{\sqrt{\sigma_{vh}^0 \sigma_{vv}^0}}. \quad (36)$$

Indeed, these coefficients result to be independent of small-scale roughness. Moreover, the coefficient $\rho_{vh,vv}$ is dependent on wind direction through the surface slope correlation coefficient ρ , i.e., according to (19), it presents oscillations of the kind $\sin(2\varphi_w)$.

E. Circular Basis

By using the well-known relations between linear and circular polarization bases [16], the elements of the backscattering circular polarization covariance matrix can be related to the linear polarization ones as follows:

$$\begin{cases}
 \sigma_{RL}^0 = \frac{1}{4} (\sigma_{hh}^0 + \sigma_{vv}^0 + 2\text{Re}\{R_{hh,vv}\}) \\
 \sigma_{RR}^0 = \frac{1}{4} (\sigma_{hh}^0 + \sigma_{vv}^0 - 2\text{Re}\{R_{hh,vv}\} + 4\sigma_{hv}^0 \\
 \quad + 4\text{Im}\{R_{hh,hv} + R_{hv,vv}\}) \\
 \sigma_{LL}^0 = \frac{1}{4} (\sigma_{hh}^0 + \sigma_{vv}^0 - 2\text{Re}\{R_{hh,vv}\} + 4\sigma_{hv}^0 \\
 \quad - 4\text{Im}\{R_{hh,hv} + R_{hv,vv}\}) \\
 R_{RR,LL} = \frac{1}{4} [- (\sigma_{hh}^0 + \sigma_{vv}^0 - 2\text{Re}\{R_{hh,vv}\}) \\
 \quad + 4\sigma_{hv}^0 - 4j\text{Re}\{R_{hh,hv} - R_{hv,vv}\}] \\
 R_{RR,RL} = \frac{-j}{4} (\sigma_{hh}^0 - \sigma_{vv}^0 + 2j\text{Im}\{R_{hh,vv}\} \\
 \quad + 2j\{R_{hh,hv}^* + R_{hv,vv}\}) \\
 R_{LL,RL} = \frac{-j}{4} (\sigma_{vv}^0 - \sigma_{hh}^0 - 2j\text{Im}\{R_{hh,vv}\} \\
 \quad + 2j\{R_{hh,hv}^* + R_{hv,vv}\})
 \end{cases} \quad (37)$$

where indices R and L stand for right-handed and left-handed circular polarizations, respectively.

From (37), we readily get that in the GO case only σ_{RL}^0 is nonnull and equal to the first of (21), whereas all other elements of the covariance matrix are equal to zero. With regard to SPM expressions for a tilted facet, by using (27) in (37), we get

$$\begin{cases}
 \sigma_{RL}^{0SPM} = \frac{1}{\pi} k^4 \cos^4 \vartheta_l W(2k \sin \vartheta_l) \Phi(2k \sin \vartheta_l, \varphi_l) \\
 \quad \times [|F_h(\vartheta_l)|^2 + |F_v(\vartheta_l)|^2 + 2\text{Re}\{F_h(\vartheta_l) F_v^*(\vartheta_l)\}] \\
 \sigma_{RR}^{0SPM} = \sigma_{LL}^{0SPM} = |R_{RR,LL}^{SPM}| \\
 \quad = \frac{1}{\pi} k^4 \cos^4 \vartheta_l W(2k \sin \vartheta_l) \Phi(2k \sin \vartheta_l, \varphi_l) \\
 \quad \times [|F_h(\vartheta_l)|^2 + |F_v(\vartheta_l)|^2 - 2\text{Re}\{F_h(\vartheta_l) F_v^*(\vartheta_l)\}] \\
 \arg\{R_{RR,LL}^{SPM}\} = -4\beta + \pi \\
 R_{RR,RL}^{SPM} = \frac{1}{\pi} k^4 \cos^4 \vartheta_l W(2k \sin \vartheta_l) \Phi(2k \sin \vartheta_l, \varphi_l) \\
 \quad \times \left\{ [|F_h(\vartheta_l)|^2 - |F_v(\vartheta_l)|^2 \right. \\
 \quad \left. + 2j\text{Im}\{F_h(\vartheta_l) F_v^*(\vartheta_l)\} \right\} \exp \left[-j \left(2\beta + \frac{\pi}{2} \right) \right] \\
 R_{LL,RL}^{SPM} = \frac{1}{\pi} k^4 \cos^4 \vartheta_l W(2k \sin \vartheta_l) \Phi(2k \sin \vartheta_l, \varphi_l) \\
 \quad \times \left\{ [|F_v(\vartheta_l)|^2 - |F_h(\vartheta_l)|^2 \right. \\
 \quad \left. - 2j\text{Im}\{F_h(\vartheta_l) F_v^*(\vartheta_l)\} \right\} \exp \left[j \left(2\beta - \frac{\pi}{2} \right) \right].
 \end{cases} \quad (38)$$

Finally, by using the Taylor expansions of Section III-C and averaging over s_a , s_r as in Section III-D, we obtain

$$\begin{aligned}
 \langle \sigma_{RL}^{0SPM} \rangle &= \frac{1}{4} \Theta_{hv}(\vartheta) \Phi(2k \sin \vartheta, 0) \\
 &\times \left[\frac{|F_v(\vartheta) + F_h(\vartheta)|^2}{F_h(\vartheta) F_v^*(\vartheta)} + \frac{C_{0,2}^{hh} + C_{0,2}^{vv} + 2\text{Re}\{C_{0,2}^{hv}\}}{\Theta_{hv}(\vartheta)} \sigma_r^2 \right. \\
 &\quad \left. + \frac{C_{2,0}^{hh} + C_{2,0}^{vv} + 2\text{Re}\{C_{2,0}^{hv}\}}{\Theta_{hv}(\vartheta)} \sigma_a^2 \right] \\
 \langle \sigma_{RR}^{0SPM} \rangle &= \langle \sigma_{LL}^{0SPM} \rangle = \frac{1}{4} \Theta_{hv}(\vartheta) \Phi(2k \sin \vartheta, 0) \\
 &\times \left[\frac{|F_v(\vartheta) - F_h(\vartheta)|^2}{F_h(\vartheta) F_v^*(\vartheta)} + \frac{C_{0,2}^{hh} + C_{0,2}^{vv} - 2\text{Re}\{C_{0,2}^{hv}\}}{\Theta_{hv}(\vartheta)} \sigma_r^2 \right. \\
 &\quad \left. + \frac{C_{2,0}^{hh} + C_{2,0}^{vv} - 2\text{Re}\{C_{2,0}^{hv}\}}{\Theta_{hv}(\vartheta)} \sigma_a^2 \right] \\
 \langle R_{RR,LL}^{SPM} \rangle &= -\frac{1}{4} \Theta_{hv}(\vartheta) \Phi(2k \sin \vartheta, 0) \\
 &\times \left[\frac{|F_v(\vartheta) - F_h(\vartheta)|^2}{F_h(\vartheta) F_v^*(\vartheta)} \left(1 - \frac{8\sigma_a^2}{\sin^2 \vartheta} - 4j \frac{\cot \vartheta}{\sin \vartheta} \rho \sigma_a \sigma_r \right) + \right. \\
 &\quad - j \frac{C_{0,1}^{hh} + C_{0,1}^{vv} - 2\text{Re}\{C_{0,1}^{hv}\}}{\Theta_{hv}(\vartheta) \sin \vartheta} 4\rho \sigma_a \sigma_r \\
 &\quad + \frac{C_{0,2}^{hh} + C_{0,2}^{vv} - 2\text{Re}\{C_{0,2}^{hv}\}}{\Theta_{hv}(\vartheta)} \sigma_r^2 \\
 &\quad \left. + \frac{C_{2,0}^{hh} + C_{2,0}^{vv} - 2\text{Re}\{C_{2,0}^{hv}\}}{\Theta_{hv}(\vartheta)} \sigma_a^2 \right] \\
 \langle R_{RR,RL}^{SPM} \rangle &= \frac{-j}{4} \Theta_{hv}(\vartheta) \Phi(2k \sin \vartheta, 0) \\
 &\times \left[\frac{|F_h(\vartheta)|^2 - |F_v(\vartheta)|^2 + 2j \text{Im}\{F_h(\vartheta) F_v^*(\vartheta)\}}{F_h(\vartheta) F_v^*(\vartheta)} \right. \\
 &\quad \times \left(1 - \frac{2\sigma_a^2}{\sin^2 \vartheta} - 2j \frac{\cot \vartheta}{\sin \vartheta} \rho \sigma_a \sigma_r \right) + \\
 &\quad - j \frac{C_{0,1}^{hh} - C_{0,1}^{vv} + 2j \text{Im}\{C_{0,1}^{hv}\}}{\Theta_{hv}(\vartheta) \sin \vartheta} 2\rho \sigma_a \sigma_r \\
 &\quad + \frac{C_{0,2}^{hh} - C_{0,2}^{vv} + 2j \text{Im}\{C_{0,2}^{hv}\}}{\Theta_{hv}(\vartheta)} \sigma_r^2 \\
 &\quad \left. + \frac{C_{2,0}^{hh} - C_{2,0}^{vv} + 2j \text{Im}\{C_{2,0}^{hv}\}}{\Theta_{hv}(\vartheta)} \sigma_a^2 \right] \\
 \langle R_{LL,RL}^{SPM} \rangle &= \frac{-j}{4} \Theta_{hv}(\vartheta) \Phi(2k \sin \vartheta, 0) \\
 &\times \left[\frac{|F_v(\vartheta)|^2 - |F_h(\vartheta)|^2 - 2j \text{Im}\{F_h(\vartheta) F_v^*(\vartheta)\}}{F_h(\vartheta) F_v^*(\vartheta)} \right. \\
 &\quad \times \left(1 - \frac{2\sigma_a^2}{\sin^2 \vartheta} + 2j \frac{\cot \vartheta}{\sin \vartheta} \rho \sigma_a \sigma_r \right) \\
 &\quad + j \frac{C_{0,1}^{vv} - C_{0,1}^{hh} - 2j \text{Im}\{C_{0,1}^{hv}\}}{\Theta_{hv}(\vartheta) \sin \vartheta} 2\rho \sigma_a \sigma_r \\
 &\quad + \frac{C_{0,2}^{vv} - C_{0,2}^{hh} - 2j \text{Im}\{C_{0,2}^{hv}\}}{\Theta_{hv}(\vartheta)} \sigma_r^2 \\
 &\quad \left. + \frac{C_{2,0}^{vv} - C_{2,0}^{hh} - 2j \text{Im}\{C_{2,0}^{hv}\}}{\Theta_{hv}(\vartheta)} \sigma_a^2 \right].
 \end{aligned} \tag{39}$$

As a concluding remark of this section, with regard to the range of validity of A-PTSM expressions, we note that (39),

as well as (35), do not hold for small values of the incidence angle ($\sin \vartheta$ of the order of s_r or smaller, see Section III-C). When we use them in conjunction with the first of (21) in (20) to compute copolarized NRCSs and correlation, we will multiply them by $\tanh[(\sin \vartheta / (3\sigma_r))^6]$, which very closely approximates one for $\sin \vartheta > 3\sigma_r$ and rapidly goes to zero for $\sin \vartheta < 3\sigma_r$. Also, A-PTSM (as well as SSA2) is not accurate at near-grazing incidence angles, where multiple scattering and shadowing effects become dominant. In addition, since (6) holds for wind velocity from 4 to 25 m/s, this is the range of wind velocity for which the presented formulation can be used. It should be also noted that for wind velocities of more than about 20 m/s breaking waves that are not accounted for by our model, as well as by SSA2, may play an important role in the scattering mechanism. Therefore, in conclusion we can expect that the presented approach can be safely used for wind speeds not smaller than 4 m/s and smaller than about 20 m/s.

IV. RESULTS

A. Numerical Results

In this section, we present some numerical results obtained by using the above-described A-PTSM formulation. They are aimed on one hand at illustrating the polarimetric backscattering dependence on incidence angle, frequency, and wind speed and direction; on the other hand, they are aimed at comparing A-PTSM results with measurements and with SSA2 results.

In Fig. 3 we show vv , hh , and hv NRCS as a function of the incidence angle ϑ at X-band (frequency = 10 GHz, $\varepsilon = 61-45$) for a gentle breeze ($u_{10} = 5$ m/s) and a strong wind (near gale, $u_{10} = 15$ m/s), and for up-wind ($\varphi_w = 0$) and obliquous ($\varphi_w = 45^\circ$) incidence. It must be noted that the strong wind case is the same as considered in [9, Fig. 3], so that we can directly compare our A-PTSM results with those obtained in [9] by using SSA2. It can be verified that A-PTSM results are in very good agreement with SSA2 ones; only for hv polarization A-PTSM slightly underestimates SSA2 (similar to the usual TSM). However, it must be underlined that our A-PTSM formulation is completely in closed form (including expressions of slope variances), so that no numerical integral evaluation is needed, and the whole plots of our Fig. 3 are obtained in a time of the order of the second with a common laptop. Conversely, SSA2 of [9] requires the cumbersome evaluation of fourfold integrals, with highly oscillating integrands, so that they must be performed via a refined numerical method specially devised in [9].

In Fig. 4, we show RR and RL NRCS in the same cases of Fig. 3. Also in this case, A-PTSM results are in very good agreement with SSA2 ones reported in [9].

Behaviors of copolarized hh , vv and crosspolarized vh , vv correlation coefficients $\rho_{hh,vv}$ and $\rho_{vh,vv}$ are displayed in Fig. 5 in the same cases of Figs. 3 and 4. It is useful to remind that these correlation coefficients would be always unitary and undefined, respectively, according to SPM without random facet tilt.

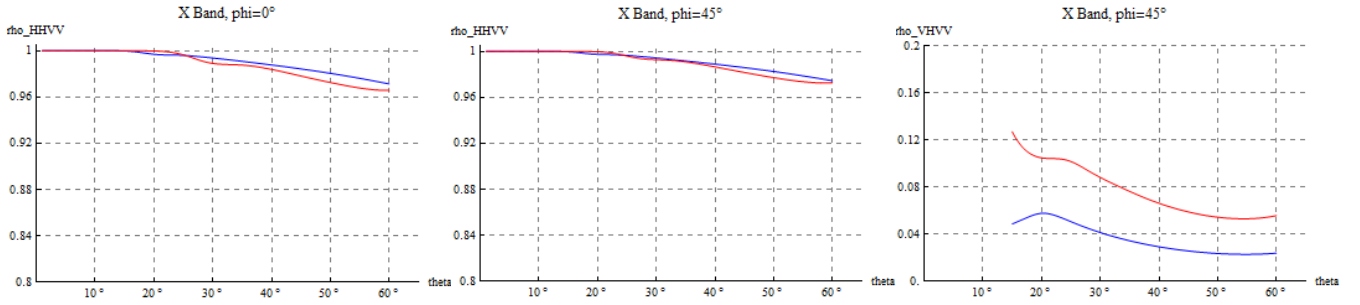


Fig. 5. Modulus of copolarized hh , vv (left and middle panels) and crosspolarized vh , vv (right panel) correlation coefficients as a function of the incidence angle ϑ at X-band (frequency = 10 GHz, $\varepsilon = 61 - j45$) for a gentle breeze ($u_{10} = 5$ m/s, blue lines) and a strong wind ($u_{10} = 15$ m/s, red lines), and for up-wind ($\varphi_w = 0$) and obliquus ($\varphi_w = 45^\circ$) incidence. Crosspolarized correlation coefficient is zero for $\varphi_w = 0$.

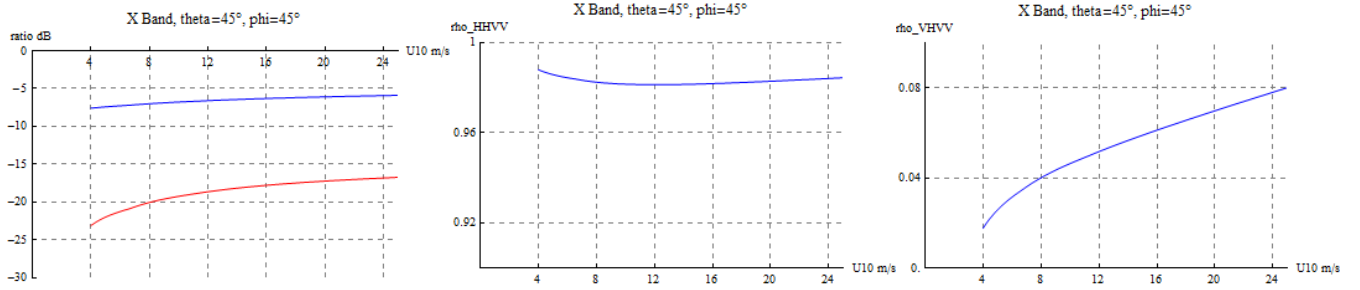


Fig. 6. Copolarized ratio $\sigma_{hh}^0/\sigma_{vv}^0$ (left panel, blue line), crosspolarized ratio $\sigma_{vh}^0/\sigma_{vv}^0$ (left panel, red line), modulus of the copolarized correlation coefficient (middle panel) and modulus of the crosspolarized correlation coefficients (right panel), as a function of wind velocity, at X-band (frequency = 10 GHz, $\varepsilon = 61 - j45$), with $\vartheta = 45^\circ$ and $\varphi_w = 45^\circ$.

In Fig. 6 we illustrate the dependence on wind intensity of copolarized and crosspolarized ratios (i.e., ratios of hh to vv , and hv to vv , NRCS) and of copolarized and crosspolarized correlation coefficients, again at X-band, with $\vartheta = 45^\circ$ and $\varphi_w = 45^\circ$. It is worth recalling that the copolarized ratio would be independent of wind speed according to SPM without random tilt, and crosspolarized ratio would be null according to that model.

Finally, in Figs. 7 and 8, we illustrate the dependence on wind direction φ_w of vv , hh , and hv NRCS and of the crosspolarized correlation coefficient for a fresh breeze ($u_{10} = 10$ m/s). In Fig. 7, we consider C band (frequency = 5.66 GHz, $\varepsilon = 67 - j36$) and $\vartheta = 35^\circ$, whereas in Fig. 8, we consider Ku band (frequency = 12.5 GHz, $\varepsilon = 42 - j39$) and $\vartheta = 45^\circ$. In these two cases, experimental data are available: for the C-band case, measurements obtained from RADARSAT-2 quad-pol SAR data are reported in [17], and for the Ku-band case, measurements obtained by using an aircraft polarimetric scatterometer are reported in [18]. Both sets of data were used in [9] to compare SSA2 and TSM results with them, and we here compare our A-PTSM results with them. At both frequencies, good agreement between A-PTSM and experimental data is obtained for vv NRCS and real part of the crosspolarized correlation coefficient. Discrepancies with hh NRCS experimental data (especially at up-wind incidence), as well as with the imaginary part of the experimental crosspolarized correlation coefficient, are very similar to those obtained by SSA2 and exact TSM in [9], and can be therefore explained as in [9]. With regard to

the hv NRCS, an underestimation of A-PTSM results with respect to experimental data by 4 to 6 dB is obtained, in agreement with exact TSM results reported in [9], whereas SSA2 results reported in [9] are in better agreement with measurements (although they also show a slight underestimation). This was expected, and it is related with the fact that A-PTSM (as well as usual TSM) does not account for multiple scattering, at variance with SSA2. This issue is better explored in Section IV-B. However, we underline again that A-PTSM, at variance with both SSA2 and exact TSM, does not require any numerical integration.

Finally, we note in Figs. 7 and 8, the $\cos(2\varphi_w)$ dependence of copolarized NRCSs, the “smoothed” $\cos(2\varphi_w)$ dependence of crosspolarized NRCS, and the $\sin(2\varphi_w)$ dependence of the crosspolarized correlation coefficient. This is in agreement with theoretical expectations highlighted at the end of Section III-D.

B. Comparison With SSA2-A

As already mentioned, in [10], an analytical approximation of SSA2 (SSA2-A) was obtained, although for the crosspolarized NRCS only, and it was shown that it is in very good agreement with exact SSA2 for moderate slopes and intermediate incidence angles. With our notation, SSA2-A crosspolarized NRCS can be expressed as

$$\sigma_{hv}^{0\text{SSA2-A}} = \frac{16}{\pi} k^4 \sin^4 \vartheta |G_\gamma(\vartheta)|^2 \cot^2 \vartheta W_{2D}(2k \sin \vartheta, 0) \sigma_a^2 \quad (40)$$

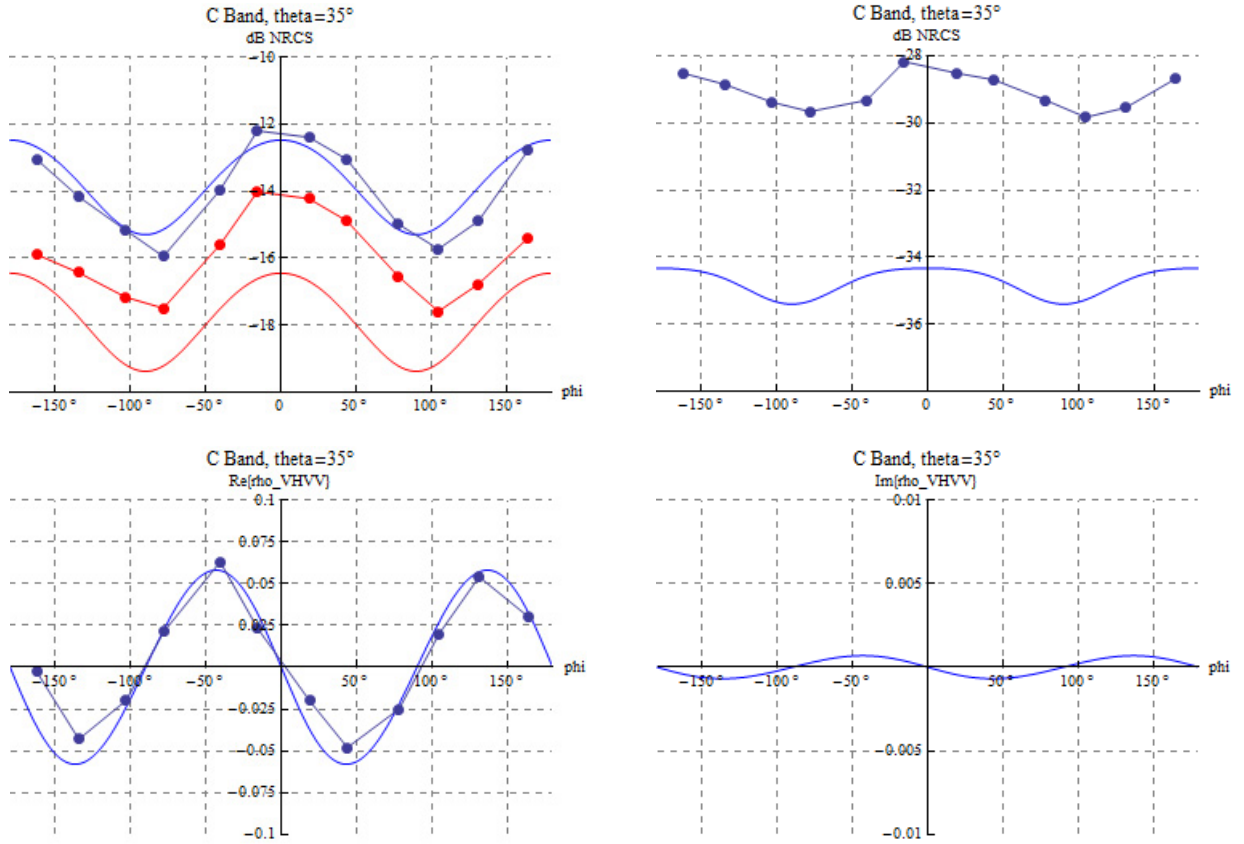


Fig. 7. Scattering dependence on wind direction φ_w at C band (frequency = 5.66 GHz, $\varepsilon = 67 - j36$), $\vartheta = 35^\circ$, and $u_{10} = 10$ m/s. (Top left) A-PTSM vv (blue, upper line) and hh (red, lower line) NRCS and corresponding measured data (blue and red connected dots). (Top right) A-PTSM hv NRCS (blue line) and corresponding measured data (blue connected dots). (Bottom left) Real part of the vh , vv correlation coefficient (blue line) and corresponding measured data (blue connected dots). (Bottom right) Imaginary part of the vh , vv correlation coefficient (blue line); corresponding measured data are mostly higher than 0.01 in magnitude and are not reported.

where

$$G_\gamma(\vartheta) = j \frac{(\varepsilon - 1)^2}{\varepsilon + \sqrt{\varepsilon}} \times \frac{\cos \vartheta \sqrt{\varepsilon - \sin^2 \vartheta}}{(\varepsilon \cos \vartheta + \sqrt{\varepsilon - \sin^2 \vartheta})(\cos \vartheta + \sqrt{\varepsilon - \sin^2 \vartheta})} \times \left(1 + \frac{3}{2} \sin^2 \vartheta \frac{\varepsilon^{1.5} + 1}{\varepsilon^{1.5} + \varepsilon} \right). \quad (41)$$

In addition, A-PTSM crosspolarized NRCS, i.e., the third line of (35), can be more explicitly expressed as

$$\sigma_{hv}^{0 \text{ A-PTSM}} = \frac{4}{\pi} k^4 \cos^4 \vartheta \left| \frac{F_v(\vartheta) - F_h(\vartheta)}{\sin \vartheta} \right|^2 \times W_{2D}(2k \sin \vartheta, 0) \sigma_a^2. \quad (42)$$

By using (40) and (42) we can obtain an analytical closed-form expression of the ratio of crosspolarized NRCSs obtained by SSA2-A and A-PTSM

$$\frac{\sigma_{hv}^{0 \text{ SSA2-A}}}{\sigma_{hv}^{0 \text{ A-PTSM}}} = \frac{4|G_\gamma(\vartheta)|^2 \sin^4 \vartheta}{|F_v(\vartheta) - F_h(\vartheta)|^2 \cos^2 \vartheta}. \quad (43)$$

This ratio turns out to be a function of only surface relative dielectric constant ε and incidence angle ϑ , while it is

independent of surface roughness and of frequency (apart from the frequency dependence of ε). For a perfectly conducting rough surface ($|\varepsilon| \rightarrow \infty$), it simplifies as

$$\frac{\sigma_{hv}^{0 \text{ SSA2-A}}}{\sigma_{hv}^{0 \text{ A-PTSM}}} = \left(1 + \frac{3}{2} \sin^2 \vartheta \right)^2 \cos^2 \vartheta. \quad (44)$$

Plots of the ratio in (43) and (44) for different values of ε are displayed in Fig. 9. They show that for any values of surface dielectric constant ε and incidence angle ϑ (except for near grazing angles), the difference of results of the two methods is not larger than about two dB. In particular, for incidence angles up to about 60° A-PTSM underestimates crosspolarized backscattering with respect to SSA2-A, since A-PTSM does not account for multiple scatterings. Conversely, for very high incidence angles (i.e., at grazing incidence), A-PTSM overestimates crosspolarized backscattering with respect to SSA2-A, most likely because it also does not account for shadowing. This latter conjecture is also supported by the fact that overestimation increases as dielectric constant, and hence shadowing, increases.

It is finally worth noting that similar results have been very recently reported in [19] for a numerical comparison of TSM and SSA2-A. Also in [19], a second-order expansion of TSM was used, but expansion coefficients were there computed

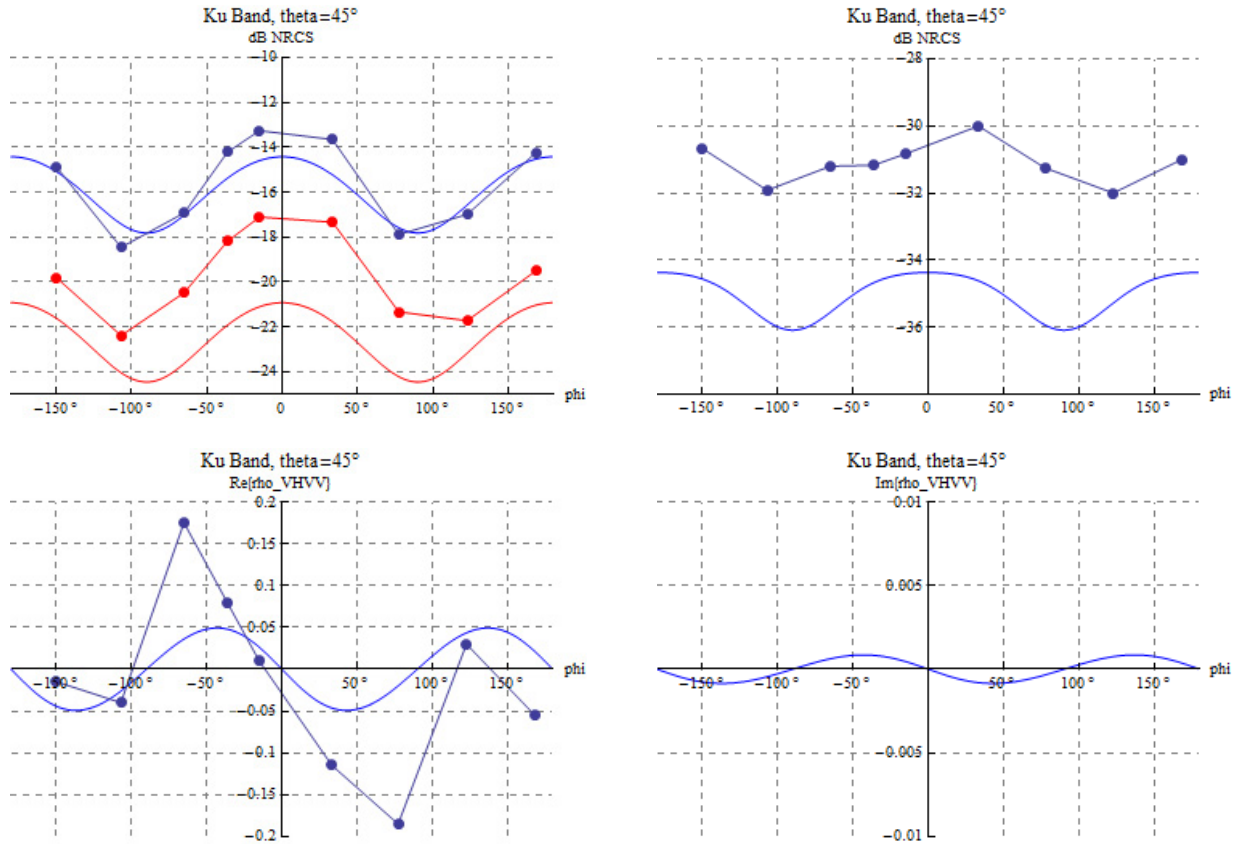


Fig. 8. Scattering dependence on wind direction ϕ_w at Ku band (frequency = 12.5 GHz, $\epsilon = 42 - j39$), $\vartheta = 45^\circ$, and $u_{10} = 10$ m/s. (Top left) A-PTSM vv (blue, upper line) and hh (red, lower line) NRCS and corresponding measured data (blue and red connected dots). (Top right) A-PTSM hv NRCS (blue line) and corresponding measured data (blue connected dots). (Bottom left) Real part of the vh , vv correlation coefficient (blue line) and corresponding measured data (blue connected dots). (Bottom right) Imaginary part of the vh , vv correlation coefficient (blue line); corresponding measured data are mostly higher than 0.01 in magnitude and are not reported.

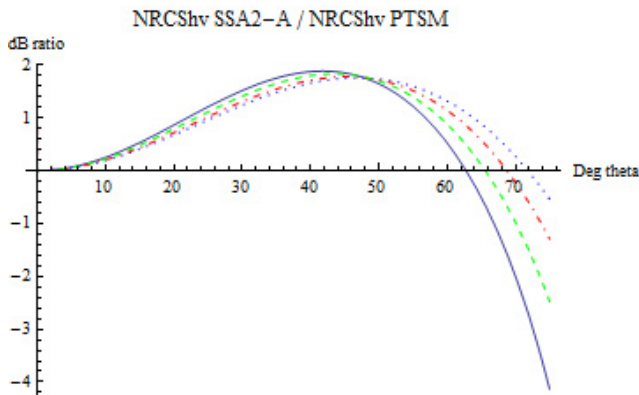


Fig. 9. Ratio, in dB, of crosspolarized NRCSs obtained by SSA2-A and A-PTSM as a function of incidence angle and for $\epsilon = 5$ (light blue dotted line), $\epsilon = 15$ (red dotted-dashed line), $\epsilon = 80$ (green dashed line), and perfectly conducting surface (blue solid line).

numerically, so that no closed-form expression comparable to (43) and (44) was there obtained.

V. CONCLUSION

We have extended the PTSM to deal with scattering surfaces with anisotropic roughness, so obtaining the A-PTSM, and we have applied it to backscattering from the sea surface. In doing

this, we have also devised an original method to easily evaluate large-scale surface slope variances as a function of wind speed and direction. All the elements of the polarimetric covariance matrix have been analytically expressed in closed form, both in the linear and in the circular polarization bases, so that no numerical integration is needed by our method. This renders all computations very fast, which is an important advantage in situations in which scattering must be computed several times, such as in implementing inversion methods for the retrieval of surface parameters. In addition, although obtained closed-form expressions are rather lengthy, some direct insight into the scattering dependence on wind speed and direction can be gained, see the end of Section III-D.

Obtained results are in good agreement with SSA2 results and experimental data. Only for the crosspolarized NRCS, A-PTSM results show a nonnegligible underestimation with respect to SSA2 results and experimental data. In order to better investigate this discrepancy, we have analytically evaluated in closed form the ratio of crosspolarized NRCSs obtained by SSA2-A (an analytical approximation of SSA2 only available for the crosspolarized NRCS) and A-PTSM. The obtained expression shows that this ratio is a function of only surface relative dielectric constant and incidence angle, while it is independent of surface roughness, and that the difference of results of the two methods is not larger than about two dB in

the range of incidence angles of interest in many applications (i.e., intermediate incidence angles).

In conclusion, we can state that for applications in which computational efficiency is important (for instance, wind speed and direction retrieval, or, more in general, surface parameter retrieval) A-PTSM is certainly preferable for all the elements of the covariance matrix, except for the crosspolarized NRCS, for which SSA2-A can be used with equal efficiency and even greater accuracy.

Finally, we explicitly note that, although here we have applied A-PTSM to scattering from a sea surface described by the directional Elfouhaily spectrum, the formulations of (35) and (39) can be used, with no need of recalculating the expressions of expansion coefficients $C_{k,n-k}^{pq}$, for any small-scale roughness PSD in the form of (1), provided that, in the range of surface wavenumbers of interest for microwave scattering, $W(\kappa)$ can be approximated by a power-law function and $\Phi(\kappa, \varphi)$ can be approximated as $\Phi(\kappa, \varphi) \cong \Phi(\varphi) = 1 + \Delta \cdot f(\varphi)$, where $f(\varphi)$ must be periodic of period π , with null average over the period, $\max\{|f(\varphi)|\} = 1$, and Δ is assumed to be much smaller than unity. Extension to any Δ smaller than or equal to unity is not difficult, but it is left to future work. Conversely, extension of PTSM and A-PTSM to the bistatic scattering configuration is by no means straightforward, and it is left to future work, too.

APPENDIX

In this Appendix, we report the expressions of $C_{0,1}^{pq}$

$$\begin{aligned} C_{0,1}^{pq} &= \left. \frac{\partial(W(2k \sin \vartheta_l)(k \cos \vartheta_l)^4 F_p(\vartheta_l) F_q^*(\vartheta_l))}{\partial s_r} \right|_{s_a=s_r=0} \\ &= \left. \frac{\partial(W(2k \sin \vartheta_l)(k \cos \vartheta_l)^4)}{\partial s_r} F_p(\vartheta_l) F_q^*(\vartheta_l) \right|_{s_a=s_r=0} \\ &\quad + \left. W(2k \sin \vartheta_l)(k \cos \vartheta_l)^4 \frac{\partial F_p(\vartheta_l)}{\partial s_r} F_q^*(\vartheta_l) \right|_{s_a=s_r=0} \\ &\quad + \frac{1}{2} \left. W(2k \sin \vartheta_l)(k \cos \vartheta_l)^4 F_p(\vartheta_l) \frac{\partial F_q^*(\vartheta_l)}{\partial s_r} \right|_{s_a=s_r=0}. \end{aligned} \quad (45)$$

Closed-form expressions of the derivatives appearing in (45) are reported in [6, Appendix B].

REFERENCES

- [1] J. W. Wright, "A new model for sea clutter," *IEEE Trans. Antennas Propag.*, vol. AP-16, no. 2, pp. 217–223, Mar. 1968.
- [2] G. R. Valenzuela, "Scattering of electromagnetic waves from a tilted slightly rough surface," *Radio Sci.*, vol. 3, no. 11, pp. 1057–1066, Nov. 1968.
- [3] D. L. Schuler and J. S. Lee, "A microwave technique to improve the measurement of directional ocean wave spectra," *Int. J. Remote Sens.*, vol. 16, no. 2, pp. 199–215, 1995.
- [4] S. H. Yueh, "Modeling of wind direction signals in polarimetric sea surface brightness temperatures," *IEEE Trans. Geosci. Remote Sens.*, vol. 35, no. 6, pp. 1400–1418, Nov. 1997.
- [5] Y. He, W. Perrie, T. Xie, and Q. Zou, "Ocean wave spectra from a linear polarimetric SAR," *IEEE Trans. Geosci. Remote Sens.*, vol. 42, no. 11, pp. 2623–2631, Nov. 2004.
- [6] A. Iodice, A. Natale, and D. Riccio, "Retrieval of soil surface parameters via a polarimetric two-scale model," *IEEE Trans. Geosci. Remote Sens.*, vol. 49, no. 7, pp. 2531–2547, Jul. 2011.

- [7] A. Iodice, A. Natale, and D. Riccio, "Polarimetric two-scale model for soil moisture retrieval via dual-Pol HH-VV SAR data," *IEEE J. Sel. Topics Appl. Earth Observ. Remote Sens.*, vol. 6, no. 3, pp. 1163–1171, Jun. 2013.
- [8] G. Di Martino, A. Iodice, A. Natale, and D. Riccio, "Polarimetric two-scale two-component model for the retrieval of soil moisture under moderate vegetation via L-band SAR data," *IEEE Trans. Geosci. Remote Sens.*, vol. 54, no. 4, pp. 2470–2491, Apr. 2016.
- [9] A. G. Voronovich and V. U. Zavorotny, "Full-polarization modeling of monostatic and bistatic radar scattering from a rough sea surface," *IEEE Trans. Antennas Propag.*, vol. 62, no. 3, pp. 1362–1371, Mar. 2014.
- [10] C.-A. Guérin and J. T. Johnson, "A simplified formulation for rough surface cross-polarized backscattering under the second-order small-slope approximation," *IEEE Trans. Geosci. Remote Sens.*, vol. 53, no. 11, pp. 6308–6314, Nov. 2015.
- [11] T. Elfouhaily, B. Chapron, K. Katsaros, and D. Vandemark, "A unified directional spectrum for long and short wind-driven waves," *J. Geophys. Res.*, vol. 102, no. C7, pp. 15781–15796, 1997.
- [12] M. R. Dhanak and N. I. Xiros, Eds., *Handbook of Ocean Engineering*. Cham, Switzerland: Springer, 2016.
- [13] C. Cox and W. Munk, "Measurement of the roughness of the sea surface from photographs of the sun's glitter," *J. Opt. Soc. Amer.*, vol. 44, no. 11, pp. 838–850, 1954.
- [14] S. J. Katzberg, O. Torres, and G. Ganoe, "Calibration of reflected GPS for tropical storm wind speed retrievals," *Geophys. Res. Lett.*, vol. 33, no. 18, pp. L18602-1–L18602-5, 2006.
- [15] L. Jong-Sen, D. L. Schuler, and T. L. Ainsworth, "Polarimetric SAR data compensation for terrain azimuth slope variation," *IEEE Trans. Geosci. Remote Sens.*, vol. 38, no. 5, pp. 2153–2163, Sep. 2000.
- [16] J.-S. Lee and E. Pottier, *Polarimetric Radar Imaging: From Basics to Applications*. Boca Raton, FL, USA: CRC Press, 2009.
- [17] B. Zhang *et al.*, "Ocean vector winds retrieval from C-band fully polarimetric SAR measurements," *IEEE Trans. Geosci. Remote Sens.*, vol. 50, no. 11, pp. 4252–4261, Nov. 2012.
- [18] S. H. Yueh, W. J. Wilson, and S. Dinardo, "Polarimetric radar remote sensing of ocean surface wind," *IEEE Trans. Geosci. Remote Sens.*, vol. 40, no. 4, pp. 793–800, Apr. 2002.
- [19] S. N. Wijesundara and J. T. Johnson, "A study of cross-polarized sea clutter using the SSA2 high frequency approximation and the two-scale model," in *Proc. IGARSS*, Valencia, Spain, 2018, pp. 57–59.



Gerardo Di Martino (S'06–M'09–SM'17) was born in Naples, Italy, in 1979. He received the Laurea degree (*cum laude*) in telecommunication engineering and the Ph.D. degree in electronic and telecommunication engineering from University Federico II, Naples, in 2005 and 2009, respectively.

From 2009 to 2016, he was with the University of Naples Federico II, focusing on projects regarding applied electromagnetics and remote sensing topics. From 2014 to 2016, he was also with the Italian National Consortium for Telecommunications, Parma, Italy, and the Regional Center Information Communication Technology, Naples. He is currently an Assistant Professor of electromagnetics with the Department of Electrical Engineering and Information Technology, University of Naples Federico II. His research interests include microwave remote sensing and electromagnetics, with a focus on electromagnetic scattering from natural surfaces and urban areas, synthetic aperture radar (SAR) signal processing and simulation, information retrieval from SAR data, and electromagnetic propagation in urban areas.

Dr. Di Martino serves as an Associate Editor for the IEEE ACCESS.



Antonio Iodice (S'97–M'00–SM'04) was born in Naples, Italy, in 1968. He received the Laurea degree (*cum laude*) in electronic engineering and the Ph.D. degree in electronic engineering and computer science from the University of Naples “Federico II,” Naples, in 1993 and 1999, respectively.

In 1995, he joined the Research Institute for Electromagnetism and Electronic Components, Italian National Council of Research, Naples, and from 1999 to 2000 he was with Telespazio S.p.A., Rome, Italy. Since 2000, he has been at the University of Naples “Federico II,” where he is currently a Full Professor of electromagnetic fields with the Department of Electrical Engineering and Information Technology. He has authored or co-authored over 300 papers, of which about 90 published on refereed journals. His research interests include microwave remote sensing and electromagnetics: modeling of electromagnetic scattering from natural surfaces and urban areas, simulation and processing of synthetic aperture radar signals, and electromagnetic propagation in urban areas.

Dr. Iodice received the “2009 Sergei A. Schelkunoff Transactions Prize Paper Award” from the IEEE Antennas and Propagation Society, for the best paper published in 2008 on the IEEE TRANSACTIONS ON ANTENNAS AND PROPAGATION. He was recognized by the IEEE Geoscience and Remote Sensing Society as a 2015 Best Reviewer of the IEEE TRANSACTIONS ON GEOSCIENCE AND REMOTE SENSING. He has been a Principal Investigator or Co-Investigator in several projects funded by European Union, Italian Space Agency, Italian Ministry of Education and Research, Campania Regional Government, and private companies. He is the Chair of the IEEE South Italy Geoscience and Remote Sensing Chapter.



Daniele Riccio (M'91–SM'99–F'14) was born in Naples, Italy. He received the Laurea degree (*cum laude*) in electronic engineering from the University of Naples Federico II, Naples, in 1989.

His career has been developing at the University of Naples Federico II. He is a Full Professor of electromagnetic fields with the Department of Electrical Engineering and Information Technology. He was a Research Scientist with the Italian National Research Council at the Institute for Research on Electromagnetics and Electronic Components, Naples, from 1989 to 1994, a Guest Scientist with the German Aerospace Centre (DLR), Munich, Germany, from 1994 to 1995, and a Research Affiliate with NASA, Washington, DC, USA, from 2010 to 2018. He taught abroad as a Lecturer to the Ph.D. programme with the Universitat Politècnica de Catalunya, Barcelona, Spain, in 2006, and with Czech Technical University, Prague, Czech Republic, in 2012. He is a member of the Cassini Radar Science Team. He is the Coordinator of the Ph.D. School in Information Technology and Electrical Engineering with the University of Napoli Federico II, where he is the Representative within the Assembly of the National Inter-University Consortium for Telecommunications, and the Scientific Board of the Italian Society of Electromagnetism, where he is appointed with the Secretary role. He has authored three books, including *Scattering, Natural Surfaces, and Fractals* (2007), and over 400 scientific papers. His research interests include remote sensing, electromagnetic scattering from complex media and surfaces, synthetic aperture radar techniques, application of fractal geometry to remote sensing, propagation of electromagnetic fields for wireless communication networks.

Dr. Riccio serves as an Associate Editor for some journals on Remote Sensing. He was the General Chair of the 5G International PhD School in 2018. He was the recipient of the 2009 Sergei A. Schelkunoff Transactions Prize Paper Award for the best paper published in 2008 on the IEEE TRANSACTIONS ON ANTENNAS AND PROPAGATION.